Shortwave reflected energy from NISTAR and the Earth Polychromatic Imaging Camera onboard the DSCOVR spacecraft

Clark J. Weaver[12], Jay Herman[13], Alexander Marshak[4],
Steven R Lorentz[5], Yinan Yu[5], Allan W Smith[5], Adam Szabo[6]

[1]Atmospheric Chemistry and Dynamics Branch, NASA Goddard Space Flight Center
[2]Earth System Science Interdisciplinary Center (ESSIC), U. Maryland.
[3]Joint Center for Earth Systems Technology (JCET), U. Maryland.
[4]Climate and Radiation Laboratory, NASA Goddard Space flight Center
[5]L-1 Standards and Technology, Inc., Manassas, VA US
[6]Heliospheric Physics Laboratory, NASA Goddard Space flight Center

Correspondence to: Clark Weaver (clark.j.weaver@nasa.gov)

Abstract. We describe a new method for estimating the total reflected shortwave energy from the Earth Polychromatic Imaging Camera (EPIC) and compare it with direct measurements from the NIST Advanced Radiometer (NISTAR) instrument (Electrical substitution radiometer) – both are onboard the Lagrange-1 orbiting Deep Space Climate Observatory (DSCOVR). The 6 narrow-band wavelength channels (340 to 780nm) available from EPIC provide a framework for estimating the integrated spectral energy for each EPIC pixel. The Airborne Visible/Infrared Imaging Spectrometer (AVIRIS) and the SCIAMACHY instrument provide spectral information away from the EPIC wavelengths, particularly for wavelengths longer than 780 nm. The total area-weighted reflected shortwave energy from an entire EPIC image is compared with co-temporal Band B Shortwave reflected energy observed by NISTAR. Our analysis from March to December 2017 shows the two are highly correlated with differences ranging from -10 to 10 Watts m^{-2}. The offset bias over the entire period is less than 0.2 Watts m^{-2}. We also compare our EPIC energy maps with the Clouds and the Earth's Radiant Energy System (CERES) Single Scanner Footprint (SSF) Shortwave (SW) reflected energy observed within 3 hours of an EPIC image. Our EPIC-AVIRIS SW estimate is 5-20% higher near the EPIC image center and 5-20% lower near the image edges compared with the CERES SSF.

1. Introduction

Accurate measurements of the reflected shortwave radiation from Earth are important for understanding the Earth's radiation budget, the validation of climate models, and the evaluation of any future solar radiation management experiments. Since 2000, the Clouds and the Earth's Radiant Energy System (CERES) instruments (Wielicki et al., 1996; Loeb et al., 2016) have provided continuous global top-of-atmosphere (TOA) reflected shortwave radiation measurements from polar orbiting satellites. CERES radiances (Wm^{-2} sr^{-1}) are directional measurements. To convert to a shortwave reflected TOA flux (or irradiance, Wm^{-2}) a set of Angular Distribution Models (ADM) is used to account for the anisotropy of the field of view (FOV) scene (Loeb et al., 2003). To estimate the energy reflected

from the entire sun-lit Earth disk many high spatial resolution (20km) flux measurements, taken at different times must be aggregated together. Recently, NASA deployed the NIST Advanced Radiometer (NISTAR) instrument onboard the Deep Space Climate Observatory (DSCOVR) near the Lagrange-1 (L_1) gravitational balance point to measure instantaneous broadband short wavelength (0.2 to 4 microns), near-infrared (0.7 to 4 microns) and total

5   radiation (Valero et al., 2021, Carlson et al., 2019). It's almost stable location at L_1 point (1.6 million kilometers from Earth) means that a single measurement instantaneously captures all reflected radiation in the direction of NISTAR from almost all the sunlit side of the Earth. Also, on the DSCOVR spacecraft is the Earth Polychromatic Imaging Camera (EPIC) obtaining images from the sunlit side of the Earth 10-22 times per day.

10   Even though the CERES and NISTAR estimates of the reflected earth radiation involve entirely different approaches, they should be within the uncertainties of each instrument. Instead, global annual daytime mean SW fluxes from NISTAR are about 6 % greater than those from CERES (Su et. al 2020). A previously published estimate of the shortwave broadband reflected energy from calibrated EPIC images are within the CERES calibration and algorithm uncertainties (Su et. al 2018) suggesting issues with the NISTAR measurements. This

15   approach uses narrowband-to-broadband regressions using both MODIS and TOA fluxes from CERES. A third approach regresses the CERES fluxes with ten EPIC channels and bases the comparison on the residuals from the regression analysis (Lim Y.K. et al 2021).

This work describes a new approach to derive shortwave reflected energy from the calibrated EPIC data that is

20   independent of CERES fluxes, CERES Angular Distribution Models (ADM) or MODIS observations. Our method uses additional spectral information from the EPIC 780nm channel as well as the two ultraviolet channels, 340 and 388 nm. To estimate the spectral energy between the narrow-band channels and beyond 780nm in the near infrared, hyperspectral information from both the Airborne Visible/Infrared Imaging Spectrometer (AVIRIS) aircraft measurements (Green et al., 1998) and the SCanning Imaging Absorption spectroMeter for Atmospheric

25   CHartographY (SCIAMACHY) (Bovensmann, et al., 1999) are used.

2. Methodology

2.1 EPIC

30   The EPIC camera focuses sun-lit images of earth on a 2,048 × 2,048 pixel CCD (Charge Coupled Device) detector at 10 narrow-band wavelengths from 317 to 780nm (Herman et al., 2018, Marshak et al, 2018). Our study uses six channels (two UV and four visible) over ocean; and four visible over land scenes. The chosen wavelengths have minimal gas absorption and can be used for estimating total reflected energy. The effective pixel spatial resolution at nadir is approximately 18km and increases with viewing angle. We use calibrated radiances (Herman et al., 2018,

35   Geogdzhayev & Marshak, 2018) from each EPIC pixel.

2.2 NISTAR

The National Institute of Standards and Technology Advanced Radiometer (NISTAR) instrument consists of three Electrical substitution radiometers that measure: Shortwave, Near-Infrared and Total irradiance, over a narrow cone (1° Field Of View (FOV), and 7° field of regard) that includes the full sun-lite portion of the Earth. Radiances used in this study are calculated from the Earth reflected irradiance measurements and the solid angle determined from the FOV.

5

The radiometer assigned to the Shortwave portion of the spectrum sees reflected earth radiation after passing through a broadband (0.2–4.0 μm) filter. Since the filter has a SW transmission less than one, a calibration factor must be applied to the measured radiances, to produce unfiltered radiances. The archived Level 1B BandB SW radiances used in this study are converted to unfiltered values by multiplying them by 1.15075 (1.0/0.8690) to account for photons absorbed by the filter.

10

2.3 AVIRS and SCIAMACHY

The Airborne Visible/Infrared Imaging Spectrometer (AVIRIS) provides simultaneous images of upwelling spectral radiance for 224 contiguous spectral channels with wavelengths from 400 to 2500 nm. The NASA ER-2 is the AVIRIS platform of choice for our study since it is closest to the TOA and has a spatial resolution of 20 meters. We sifted through the many AVIRIS flights and selected nadir viewed spectra from 10 homogeneous scenes: 1) a solid cloud scene with near 100% cloud fraction; 2) a cloud-free ocean scene; 3 through 10) eight different scenes over land based on the measured Normalized Difference Vegetation Index NDVI (see Table 1).

15

20

Table 1. Details of ten homogeneous AVIRIS scenes

		Latitude Longitude	Solar Elevation	Flight Number
Solid **Cloud Spectra**		37.6, -119.1	33	f150127t01p00r07
Ocean Spectra Monterey CA		36.8, -122.1	35	f131030t01p00r07
Land Spectra	NDVI			
California Yellow_Desert_0	0.0	35.6, -115.1	32	f171206t01p00r12
Arizona Desert_1	0.1	36.0, -113.3	32	F171206t01p00r08
Arizona Desert_1a	0.1	36.0, -113.3	32	F171206t01p00r08
Arizona Desert_2	0.2	36.0, -113.3	32	F171206t01p00r08
Arizona Desert_3	0.3	36.0, -113.3	32	F171206t01p00r08
Quebec Boreal Forest_6	0.6	49.8, -74.3	49	F080721t01p00r08
Quebec Boreal Forest_7	0.7	49.8, -74.3	49	F080721t01p00r08
Hawaii Tropical Veg_8	0.8	19.2, -155.3	45	F180118t01p00r16

Our method assumes that the spectra from a given EPIC pixel can be modeled by a linear combination of the spectra from selected pairs of these homogeneous scenes. Over ocean the EPIC pixel is modeled by a linear combination of the solid cloud scene with the clear-ocean scene. Over land the combination is the solid cloud scene with one of the eight cloud-free land scenes. To account for pixels over lakes or rivers the solid cloud scene can be linearly combined with the clear-ocean scene.
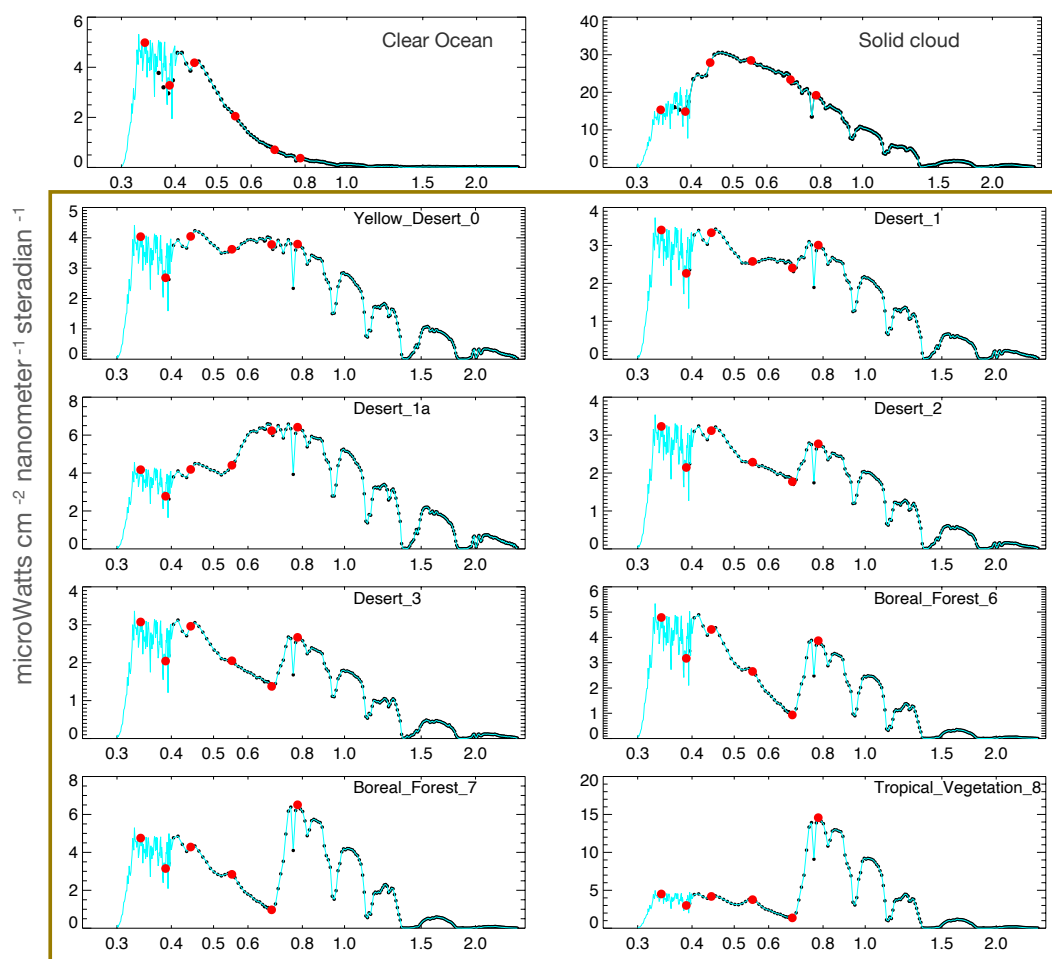

Figure 1. Spectra from the ten homogeneous scenes used to estimate SW reflected energy from EPIC. The visible and near IR portion is from AVIRIS spectra (black dots) and the UV is from SCIAMACHY when viewing a similar scene type. Since, SCIAMACHY and AVIRIS scenes are not collocated, SCIAMACHY radiances are adjusted to the AVIRIS viewing geometry. Then the SCIAMACHY radiances are scaled to match AVIRIS between 400-450nm. The SCIAMACHY contribution is shown below 450mn and the AVIRIS above 450nm, both in light blue. The six EPIC channels used to estimate the SW reflected energy are shown by the red circles. Note that the AVIRIS spectra below 400nm is not used in our study. The numbers in the spectra label are roughly related to 10*NDVI determined from the 680 and 780nm radiances so Tropical_Vegetation_8 has NDVI~0.8 . The eight clear sky land scene types are within the brown box.

The AVIRIS does not get all the credit for providing the hyperspectral information, since it lacks energy in the UV wavelengths less than 400nm. Spectra from similar homogeneous scenes observed by the SCanning Imaging Absorption SpectroMeter for Atmospheric CHartographY (SCIAMACHY) instrument are merged with the AVIRIS

5 spectra to construct a complete spectrum from 275 to 2500 nm for each homogeneous scene (Figure 1). SCIAMACHY often observes parts of a spectra over different geographic locations, whereas the AVIRIS radiances at different wavelengths are simultaneous for a given FOV. Even though the AVIRIS and SCIAMACHY observations are not collocated, the spectral shapes show good agreement. Although AVIRIS UV radiances are reported below 400nm, we do not use them and use SCIAMACHY instead.

10

2.4 VLIDORT

Before comparing or merging two different spectra one needs to account for differences in viewing and illumination geometry. We generate look-up tables of radiances using the VLIDORT (Vector LInearized Discrete Ordinate Radiative Transfer package, Spurr, 2006) over the different wavelengths (275-2500nm), illumination(0-90º),

15 viewing(0-90º) and azimuthal angle (0-180º) ranges. To convert to a new viewing geometry, we scale the observed radiance from EPIC, AVIRS or SCIAMACHY by the ratio of the VLIDORT radiance at the new geometry with the VLIDORT radiance at the observed geometry.
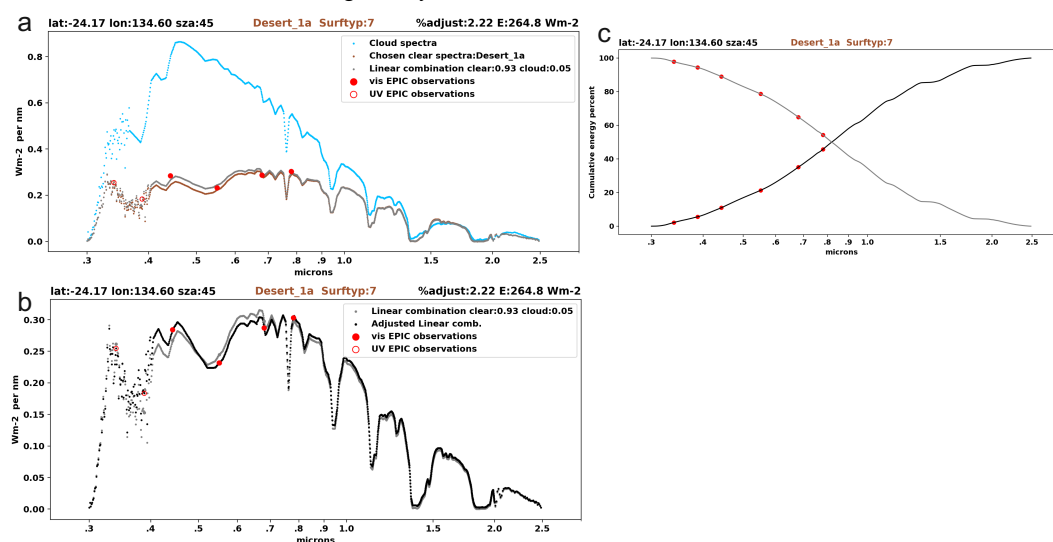
20 **Figure 2.** Construction of a composite spectrum for a single EPIC pixel viewing the central Australian open shrubland. (**a**) The grey trace is a linear combination of a pair of scene-homogeneous spectra that best fits the observed EPIC radiances (larger red circles). Our algorithm attempted to fit the Solid-cloud spectra (light blue) with each one of the eight possible clear land spectra (brown box Figure 1). For this pixel the Desert_1a (brown) had the best fit using a linear combination of 0.05* Solid-cloud spectra + 0.93* Desert_1a. (**b**) The linear combination is
25 adjusted to exactly match the EPIC observations (black trace). To adjust we determine the difference between the EPIC observations and the linear combination at 4 the visible wavelengths (red circles), then linearly interpolate these differences onto the higher spectral resolution wavelength grid (end points are set to zero). The interpolated

differences are then added to the linear combination. The spectrally integrated High Resolution energy (E) under the adjusted spectra (black) is shown in the upper RH corner, 264.8 Wm^{-2}. The '%adjust' is the percentage difference between the area under adjusted spectra (black) and the linear combination spectra (grey). For this pixel the area difference is 2.22%. Location of the pixel and solar zenith angle are shown in the LH corner. **(c)** Cumulative energy (%) from the start (0.3 microns) shown by black trace and from the end (2.5 microns) shown by grey trace.

2.5 Composite Spectra

Figure 2 illustrates how a composite spectrum is constructed for a single EPIC pixel over the central Australia. For this pixel our algorithm attempted a fit using the spectra from eight possible homogeneous clear-sky land scenes combined with the spectrum from the solid cloud scene. It found the best fit with the "Desert_1a" cloud-free spectra and archived the spectrally integrated total energy from the composite, yielding an estimate of the SW reflected energy for the EPIC pixel. Please see Figure 2 caption for more detail.
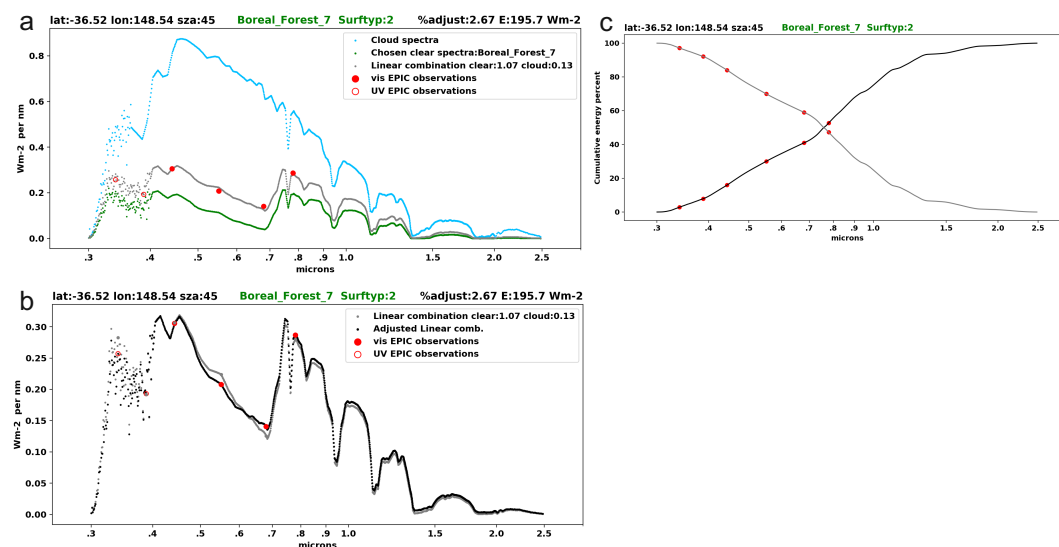
Figure 3. Construction of a composite spectrum for a single EPIC pixel over New South Wales. (**a**) The grey trace is a linear combination of a pair of scene-homogeneous spectra that best fits the observed EPIC radiances (larger red circles). Our algorithm attempted to fit the Solid-cloud spectra (light blue) with each one of the eight possible clear land spectra (brown box Figure 1). For this pixel the The Boreal_Forest_7 (green) had the best fit using a linear combination of 0.13* Solid-cloud spectra + 1.07* Boreal_Forest_7. (**b**) The linear combination is adjusted to exactly match the EPIC observations (black trace). The spectrally integrated High Resolution energy (E) under the adjusted spectra (black) is shown in the upper RH corner, 195.7 Wm^{-2}. The '%adjust' is the percentage difference between the area under adjusted spectra (black) and the linear combination spectra (grey). For this pixel the area difference is 2.67%. Location of the pixel and solar zenith angle are shown in the LH corner. **(c)** Cumulative energy (%) from the start (0.3 microns) shown by black trace and from the end (2.5 microns) shown by grey trace.

Active vegetation scenes with high NDVI values have relatively more energy in wavelengths above 680nm (Figure 3) than lower NDVI scenes. A visual comparison of the Tropical_vegitation_8 (NDVI~0.8) with lower NDVI

spectra of Figure 1 bears this out. The relative difference between the radiances at 680 and 780nm, that EPIC provides, allows our algorithm to usually choose a homogeneous AVIRIS scene that is consistent with the known land surface type. For example, EPIC pixels with Surface/biome types 1-4 (Evergreen and Deciduous Forest) usually use AVIRIS scenes with high NDVI (Boreal_Forest_7 or Tropical_Vegetation_8). Any SW broadband

5   reflected energy estimate from EPIC needs to include both the 680 and 780nm wavelengths.

3. Uncertainty

The Right Hand Side RHS legend of Figure 2b and 3b shows '%adjust' which is the difference between the energy under the final adjusted spectra (black trace) minus the linear combination spectra (grey trace). Averaging all pixels

10   for an image yields an adjustment of +0.8%. or ~2.0 Wm^{-2} and a 1σ standard deviation of 16 Wm^{-2}. While this provides some estimate of the error in the spectrally integrated energy, it does not fully account for errors in the spectral shape in the near-IR spectrum beyond 780nm. Figures 2c and 3c show that the integrated spectral energy beyond 780nm can be 50% or more of the total.

15   *3.1 Estimating near-IR energy E_{nIR} from 780nm*

Accuracy of our approach rests on the 780nm EPIC channel being able to predict the near-IR energy contribution to the total energy of a spectrum. If the surface spectra for a given EPIC pixel does not match any of the available single cloud-free AVIRIS spectra (in linear combination with the solid-cloud spectra), the adjustment of the combination spectra to the exact EPIC radiances will reduce the error in the visible contribution to the total energy.

20   However, the near-IR energy contribution (E_{nIR}) may be in inaccurate. This poor fit situation might occur if the EPIC scene is heterogeneous (e.g. forest and desert); the linear combination of two land scenes is not allowed for the current algorithm, only solid cloud with a land scene. A poor fit might also occur if the EPIC scene is snow/ice or urban; neither of these are included in the 8 available homogeneous land AVIRIS spectra.

25   *3.2 Water-Vapor*

Another source of error occurs when the water vapor column of an EPIC pixel is different than the column at the time of the AVIRIS observation. Four strong water vapor absorption bands at 0.94, 1.12, 1.39 and 1.89 microns (Ramaswamy and Freidenreich, 1991) contribute to the spectral shape in the near-IR for all the homogeneous land

30   AVIRIS spectra (Figure 1).

To investigate the ability of the 780mn EPIC measurement to predict the E_{nIR}, we consider all the nadir spectra from 10 AVIRIS flights over a variety of land surfaces (Table 2). For almost all the flights the 780nm observation accurately predicts E_{nIR} ($R^2 > 0.90$). This suggests that if our algorithm finds a land AVIRIS spectra that is consistent

35   with the spectra of the EPIC pixel, the EPIC 780nm radiance alone will be able to predict E_{nIR} with a 1σ error of ~5 Wm^{-2} (fourth column). Note that the slopes (fifth column) are sensitive to the surface type so if the algorithm cannot find a AVIRIS spectra with good fit, there will be a significant error in E_{nIR}.

5

**Table 2**. Statistics from ten AVIRIS flights over vegetation and desert scenes

N	Total number of spectra considered.
R^2	Squared correlation between observed 780nm radiance and observed spectrally integrated energy beyond 780nm (E_{nIR})
$\sigma\, E_{nIR}$	standard deviation of the residual in E_{nIR}. It is the difference between E_{nIR} calculated by spectrally integrating all AVIRIS radiances > 780nm minus E_{nIR} estimated from AVIRIS 780nm radiance using a linear fit derived from the entire flight. (e.g Figure 4a)
Slope	slope from linear fit between the observed 780nm radiance and E_{nIR}
$\sigma\, E_{wv}$	standard deviation of E_{wv}
σ NDVI	standard deviation of NDVI for entire flight

Surface scene description	N	R^2	$\sigma\, E_{nIR}$	Slope	$\sigma\, E_{wv}$	σ NDVI	Flight number
Hawaii_veg1	1736	0.98	5.1	301.	7.	0.05	f180118t01p00r16rdn_e
Hawaii_veg2	4654	0.95	5.2	305.	9.	0.04	f070127t01p00r17rdn_c
Hawaii_veg3	2668	0.91	8.6	273.	13.	0.06	f070120t01p00r03rdn_c
Hawaii_veg4	2952	0.93	6.4	284.	11.	0.06	f070120t01p00r04rdn_c
ER2_Boreal_Forest	1361	0.99	2.7	305.	7.	0.06	f080721t01p00r08rdn_c
Boreal_Forest	668	0.99	5.6	361.	12.	0.10	f080720t01p00r08rdn_c
Crop_Illinois	2623	0.91	10.5	253.	11.	0.12	f100826t01p00r05rdn_b
Crop_Mosaic	2747	0.76	6.4	135.	5.	0.16	f080713t01p00r10rdn_c
Arizona_Desert	4395	0.98	2.6	456.	5.	0.08	f171206t01p00r08rdn_e
Desert_yellow	3907	0.98	2.6	434.	4.	0.02	f171206t01p00r12rdn_e

10   To estimate the spectrally integrated energy due to water vapor absorption (E_{wv}) we consider spectra and regressions for individual flights. The surface scenes for 'Hawaii_veg2' (Figure 4) are likely homogeneous throughout the flight since there is a low variability in NDVI (1σ =0.04). Note that non-vegetation scenes have been removed using an NDIV threshold (lower portion of Figure 4c RGB image). For each AVIRS spectrum we construct a spectrum assuming there is no water vapor absorption. This hypothetical spectrum is interpolated across each of the four

15   absorption bands (see dotted blue line) and the integrated light blue shaded area is the energy absorbed by water vapor (E_{wv}). The spectra with the lowest (<25 percentile, labeled 'dry') and highest (>75 percentile labeled 'moist') values of E_{wv} are averaged and shown in grey and blue traces, respectively. The legend shows that the absolute E_{wv} and the %E_{wv} (w.r.t E_{nIR}) is higher for moist versus dry sub-sets of spectra. Since 1σ for E_{wv} and E_{nIR} (when

predicted by a 780nm radiance measurement), are similar (5.2 verus 9 Wm^{-2}), we conclude that variability in water vapor could explain a significant amount of uncertainty in E_{nIR}. One σ standard deviations of E_{wv} and E_{nIR} for all the flights (Table 2) are of similar magnitude suggesting that unaccounted water vapor variability will contribute to the uncertainty in E_{nIR}. This will also contribute to the 1σ uncertainty (16 Wm^{-2}) in EPIC SW broadband reflected

5   energy mentioned above.
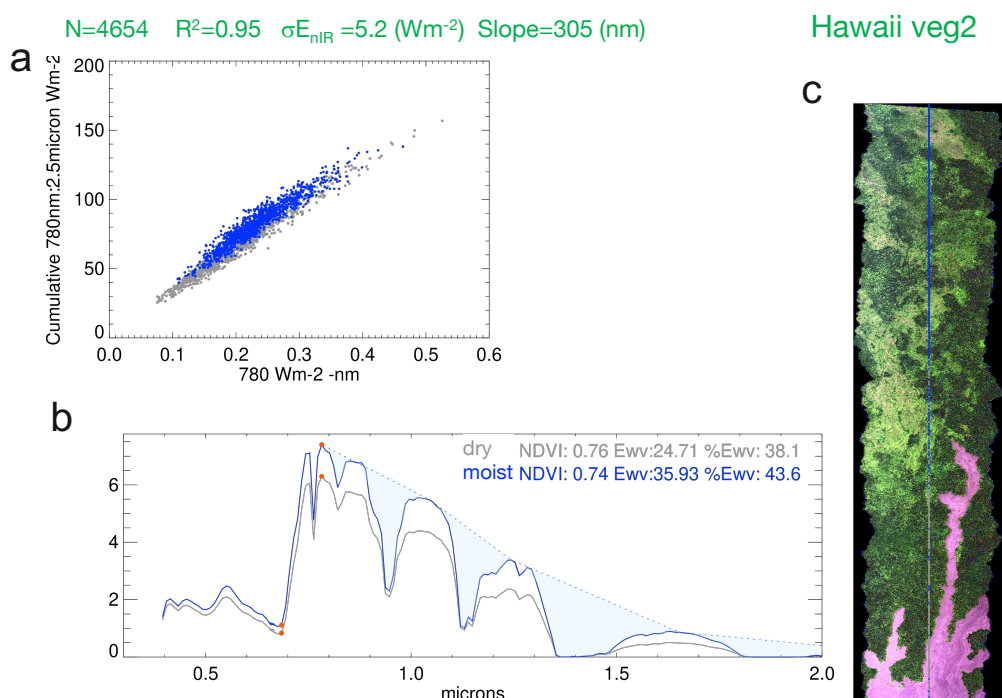
Figure 4. Flight January 27, 2007 over Hawaiian vegetation **a)** Regression of observed 780nm radiance versus observed spectrally integrated energy beyond 780nm (E_{nIR}). Values in the legend are described in Table 2 **b)** Averaged spectra for a 'moist' and 'dry' sub-set of spectra from this flight. The spectrally integrated energy due to
10   water vapor absorption (E_{wv}) is evaluated for each spectrum (see text). The 'dry' group have E_{wv} values within the first 25%ile and the 'moist' group have E_{wv} above the 75%ile. The area integral of the light blue shaded area equals E_{wv} for the 'moist' group of spectra. (Note that the solar zenith angle slowly varies during the flight leg so individual spectrum have slightly different levels of illumination. As a result, outside the water vapor bands the moist and dry groups are not expected to be identical). Red dots are radiances at wavelengths used to calculate NDVI. The legend
15   shows the average NDVI for each sub-set, the average E_{wv} and the average E_{wv} as a percentage of the near_IR energy E_{nIR} c) RGB image of flight.

4. NISTAR SW reflected energy Full Disk comparison

20   We processed all EPIC images for 2017, spatially integrated the energy from all EPIC pixels for each image, and compared the total energy with the NISTAR Band-B reflected energy. A time series of both energies (Figure 5a) shows matching annual cycle, but the diurnal cycle amplitude for NISTAR is usually larger than our EPIC estimate. The difference time series (Figure 5b) further reveals a 5 Wm^{-2} cycle. EPIC images with a higher (lower) fraction of

snow and ice are associated with negative (positive) difference values. We do not have an AVIRIS high resolution spectrum over a homogeneous snow and ice scene, so our algorithm defaults to using solid cloud spectra. We suspect that our treatment of ice scenes is deficient and may be driving the 5 Wm^{-2} cycle; we intend to include a spectrum from a homogeneous ice scene in further versions. Even with these minor issues, which average out over a single year, there is only a 0.2 Wm^{-2} bias between our EPIC estimate and the NISTAR observations. The bias is well within the ~2 Wm^{-2} error estimate of the EPIC reflected energy.
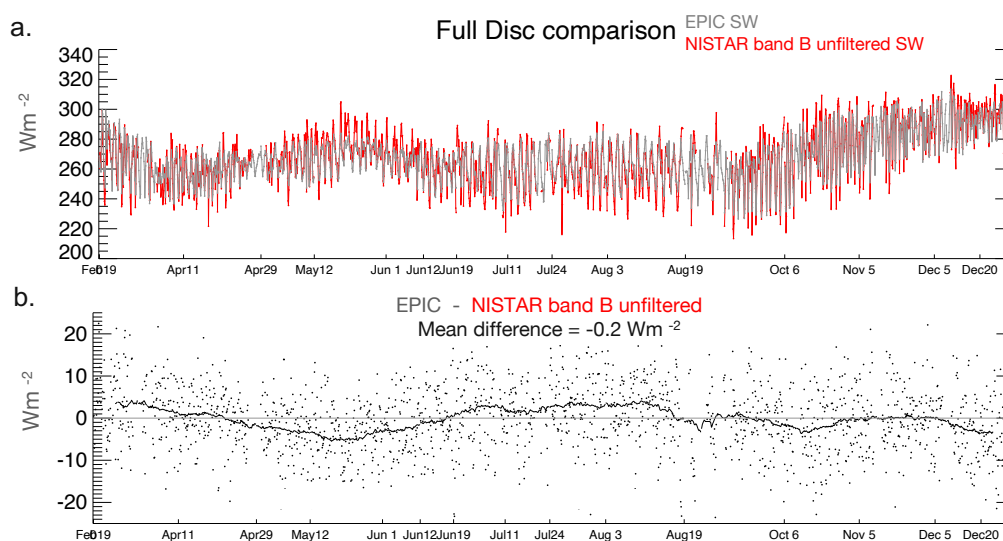
Figure 5. a) Time series of our estimate of the reflected SW energy from EPIC (grey) compared with the NISTAR Band-B reflected energy (red). **b)** EPIC SW energy minus NISTAR (black). Dots are single images and trace is 7-day smoothed difference.

5. CERES Single Scanner Footprint Partial Disk comparison

We can also compare our EPIC SW product with CERES Single Scanner Footprint (20km) Edition 4A reflected SW energy. Instead of doing a full disc comparison, we only use CERES SSF pixels that are within 1 and 3 hours of the EPIC imaging time. We use anisotropies from the Edition 2 Angular Distribution Models to convert the archived CERES flux to the energy that EPIC would observe based on the camera's viewing geometry. Both the CERES and our EPIC reflected energies are pixelated allowing map comparisons. Two different sub satellite locations over the Pacific (Figures 6) and over Africa (Figures 7) both observed on 1 June 2017 are shown.

While the synoptic patterns are remarkably similar at first glance (Figure 6&7 ab), closer examination shows that the EPIC estimates are less than CERES at the western (left) side of the earth disc. This is most apparent at cloudy locations, with energies greater than 640 Wm-2; red colored pixels occur in the CERES-AVIRS images but not the EPIC. Comparison of All EPIC-AVIRS vs. CERES SSF energy maps show this left edge disparity.
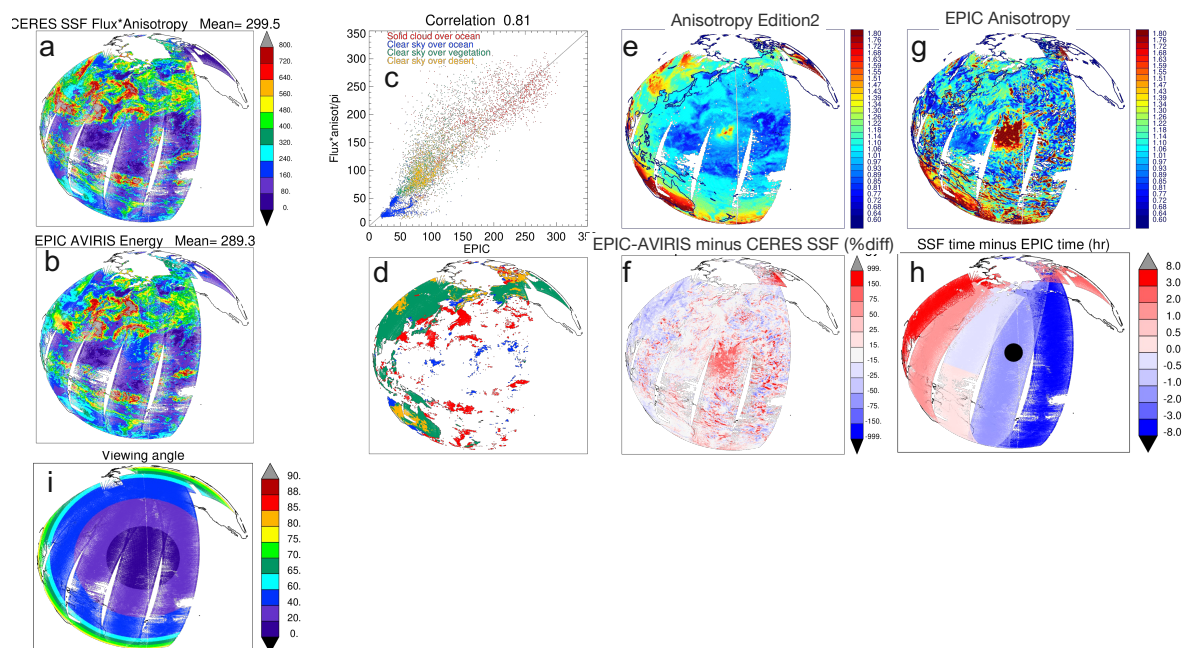
Figure 6. Maps of the SW energy from the CERES Single Scanner Footprint (SSF) **(a)** with estimates of our SW EPIC-AVIRIS reflected energy product for a single image on 1 June 2017 Hour 00 Minute 45 (**b**). To produce the CERES SSF reflected energies the SSF fluxes are multiplied by the Edition2 anisotropies consistent with the DSCOVR viewing and illumination geometry at the image time. The EPIC-AVIRIS energy is interpolated onto the SSF pixels observed within 3 hours of the EPIC image time. A scatter plot of the two different estimates of the SW energy **(c)** is color coded by four scene types: Solid cloud over Ocean (red), Clear sky over Ocean (blue) , Desert (orange) and Vegetation (green) **(d)** . Maps of anisotropies used to convert SSF SW fluxes to direction specific reflected energy **(e)** are compared with anisotropies needed to match the EPIC AVIRIS reflected energy (SW EPIC-AVIRIS energy/CERES flux) **(g)**. The % difference between EPIC-AVIRIS minus CERES **(f,)** the SSF pixel time minus the EPIC image time **(h)** and the viewing angle **(i)** are shown. The DSCOVR Solar Earth Vehicle angle is 8.88°
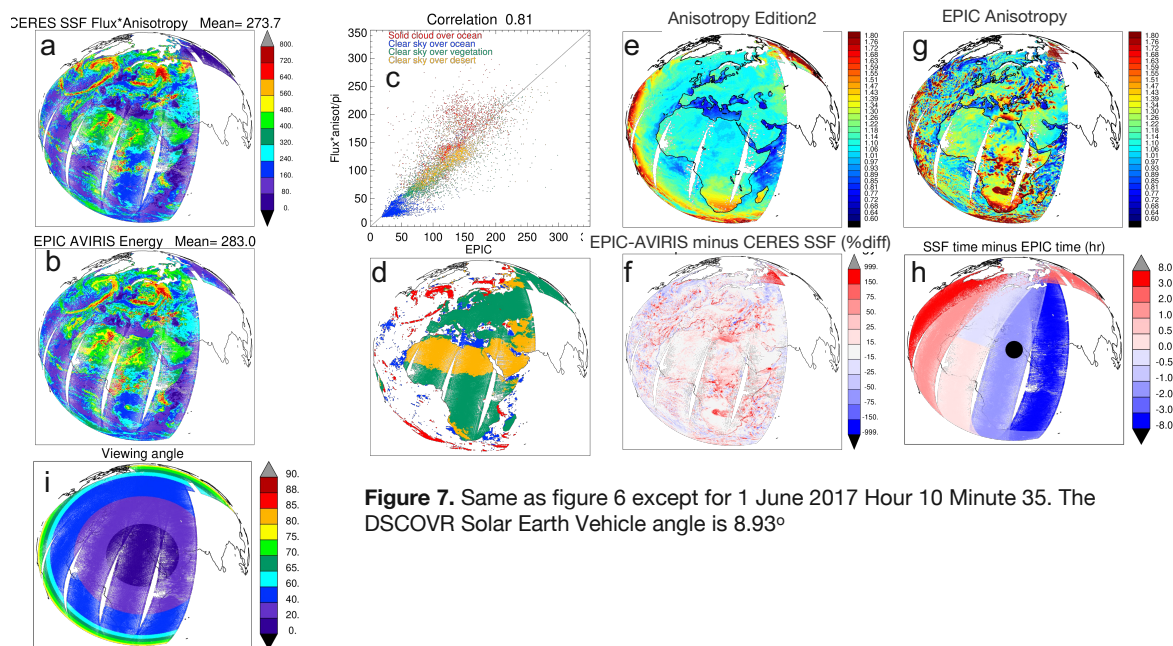
Figure 7. Same as figure 6 except for 1 June 2017 Hour 10 Minute 35. The DSCOVR Solar Earth Vehicle angle is 8.93°

5.1 Ocean glint scenes

A second general feature is that the EPIC-AVIRIS estimates significantly more reflected energy than the CERES SSF product over clear sky ocean scenes that are subject to glint conditions. A map of the percent difference (EPIC-AVRIS minus CERES, Figure 6f) shows locations with large positive percentage differences concentrated under the sub satellite point (large dot in Figure 6h). This EPIC image is featured because its sub satellite location is cloud free and over ocean, so the measured EPIC radiances at the image center are subject to sun glint conditions. RGB images on epic.gsfc.nasa.gov always show a white haze associated with glint when the subsatellite location is over clear-sky ocean.

5.2 Land and cloud scenes

A scatter plot of a subset of the pixels which are color coded by scene type (see legend of Figure 6&7 c) shows that disparities occur at all scenes over both solid cloud (red dots) and clear sky land (green and yellow dots). Note the scene type shown for a pixel is determined by our algorithm that produces the EPIC-AVIRIS energies. The accompanying map of chosen scene types (Figure 6&7 d) is consistent with the CERES surface type maps which suggests our EPIC energy algorithm is working as intended. The correlations shown in the Figure 6&7c titles (r=0.81) are determined using all pixels within 3 hours of the EPIC time and are typical for most images. When pixels are further limited to 1 hour of the EPIC time, correlations in general improve to r~0.9.

5.3 Anisotropy comparison

Maps of the CERES anisotropies (Figure 6&7 e) are compared with anisotropies that would be needed to match the EPIC-AVIRIS energies. These 'EPIC anisotropies' (Figure 6&7 g) are constructed by dividing the EPIC-AVIRIS energy by the CERES flux. While the Edition 2 anisotropies are elevated at the sun glint location, the glint location

5   and magnitude are not nearly large enough to match the EPIC-AVIRIS energy. Also, the 'EPIC anisotropies' (Figure 6g) show spatial variability not captured by the CERES anisotropy (Figure 6e) over Europe and Africa. These EPIC-AVIRIS vs CERES disparities occur at a wide range viewing angles from 0 º to 80º (Figure 6&7i).
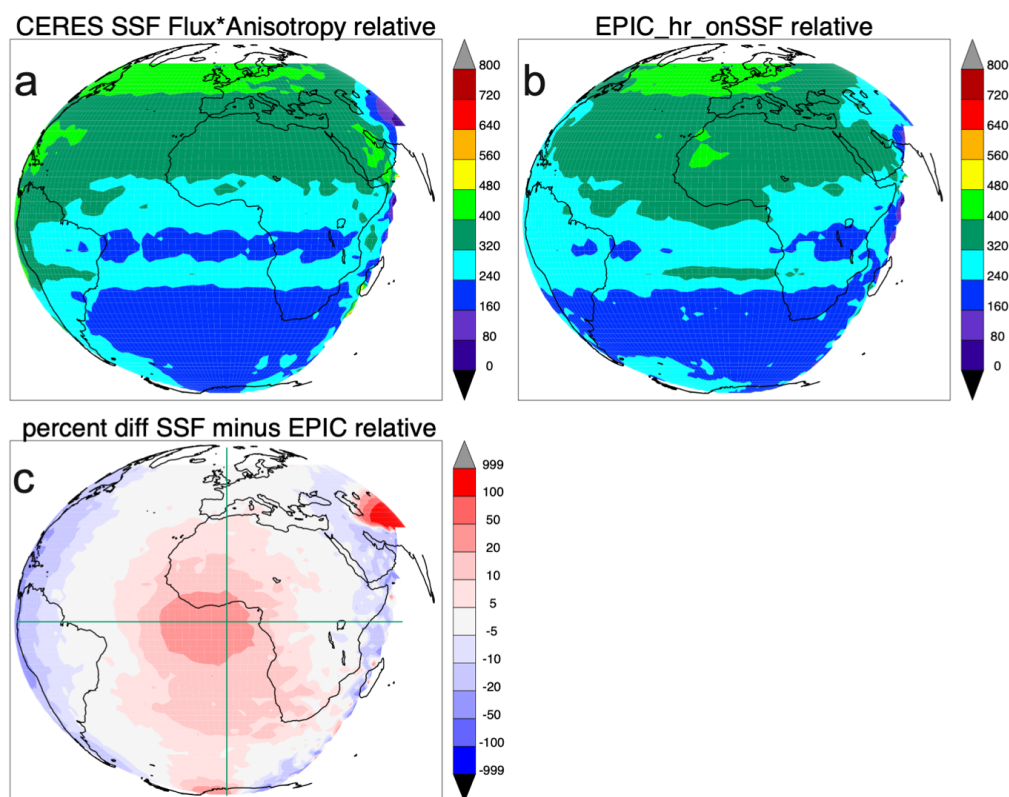

Figure 8. Composite Maps of CERES SSF **(a)** and EPIC-AVIRIS **(b)** SW reflected energy for June 2017. Prior to time averaging each image has been centered at a common subsatellite point of 0º longitude and 0º latitude. Also shown are percent differences EPIC-AVIRIS minus CERES SSF **(c)**.

10   To better understand the spatial variability of the EPIC and CERES differences we produce a time averaged map of the differences after shifting both longitude and latitude so the image's subsatellite point is 0º longitude and 0º latitude (Figure 8c). On average the EPIC-AVIRIS energy is 20% higher than the CERES SSF at the center of the earth disk and 5-20% below the CERES SSF at the edges of the earth disc. This spatial disparity means that when

SSF pixels within 3 hours of the EPIC time are used to calculate differences, the time averaged mean (3.7 Wm^{-2}, Figure 9b) will be lower than when using pixels within 1 hour of the image (9.2 Wm^{-2}, Figure 8c).
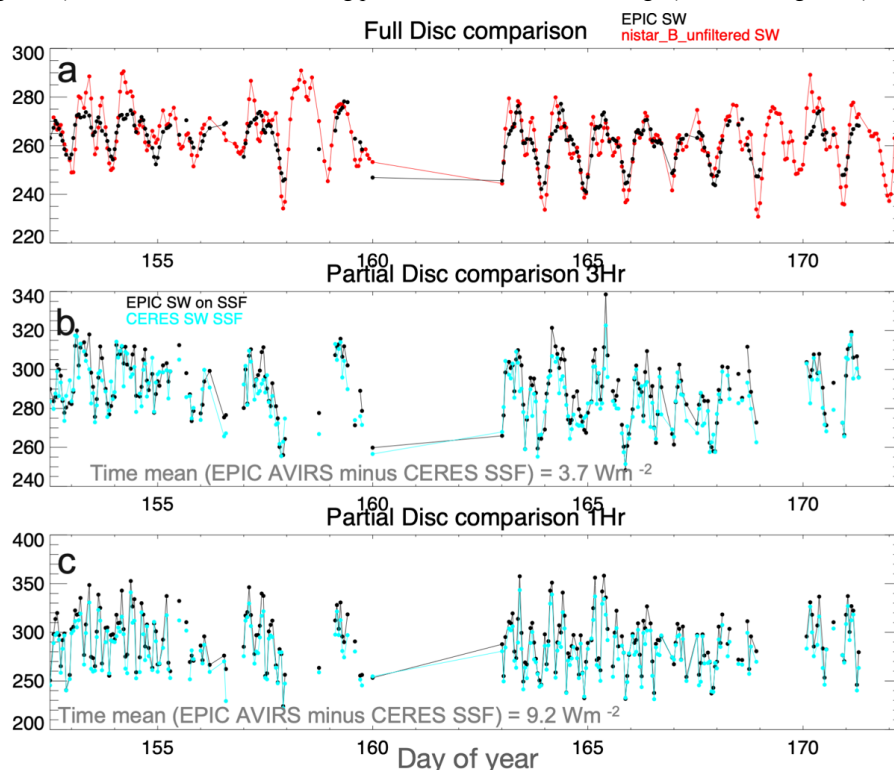

Figure 9. a) Full Disc comparison of EPIC-AVIRIS reflected SW energy (black) and the NISTAR Band-B reflected energy (red) for June 2017. **b)** Partial Disc comparison of EPIC-AVIRIS and CERES SSF using SSF pixels that are within 3 hours and **c)** within 1 hour.

5

6 Discussion

The NISTAR and EPIC instruments are both on the DSCOVER spacecraft, so they have the same illumination and near-backscattering viewing geometry. This commonality may partially explain the nice agreement between our

10 EPIC-AVIRIS reflected energy and the NISTAR band B energies shown in Figure 5. Their common geometry means that no anisotropy values, taken from Angular Distribution Models (ADM) are needed to compare the NISTAR to EPIC energies. However, comparison with the CERES fluxes requires anisotropy values at the NISTAR/EPIC near-back scattering angles, so it's a more demanding comparison. The EPIC scattering angles at each pixel are identical for a given image (angle formed between the incident and scattered-to-satellite sunlight

15 vectors). Throughout the DISCOVR mission they have ranged between 168.5° and 175.5° (180° = backscatter). The scattering angles for June 2017 are ~171°. Our results suggest there may be problems with the CERES Edition2, and likely the Edition 4 (See Appendix), Angular Distribution Models (ADM) at these near-backscatter angles. Finally,

the EPIC 780 nm wavelength information is crucial for our SW reflected energy estimate; but is not used in the CERES Langley Center team algorithm that estimates reflected energy from EPIC.

5 In summary, our EPIC-AVIRIS reflected energy product agrees with NISTAR observations, but not the CERES reflected energy; and the Langley team produced EPIC SW reflected energy product agrees with CERES, but not the NISTAR observations. Our study only addresses CERES ADMs at near-backscatter angles (~171 º), but says little about side scatter angles. To maximize spatial coverage the CERES instruments are usually in cross-track mode where observations are side scattering, far away from the near-backscatter angles we address in our study.

10 **Data availability**

All raw data can be provided by the corresponding authors upon request.

Author contributions

CW, JH, and AM formulated the research. CW coded the SW energy calculation in python. SL, AS and YY
15 provided the NISTAR data. All authors contributed to editing and reviewing the manuscript.

Competing interests

The authors declare that they have no conflict of interest.

20

Appendix

For our study we use the Edition 2 TRMM anisotropy tables downloaded from
https://ceres.larc.nasa.gov/data/angular-distribution-models/#cerestrmm-ssf-edition2b-adms
We attempt to reproduce published anisotropy maps constructed from Edition4 angular distribution models (ADM)
25 from Su et al. 2021. The similarity of the two Editions, shown in Figure A-1, suggests that we are implementing the ADM tables correctly, but also to demonstrate that the difference in Editions can only explain part of the disparities we observe. Yes, the area subject to glint has higher Edition 4 anisotropies than the Edition 2, but they are not close to the high (>1.6) values shown by the 'EPIC anisotropy' map (Figure 6g).
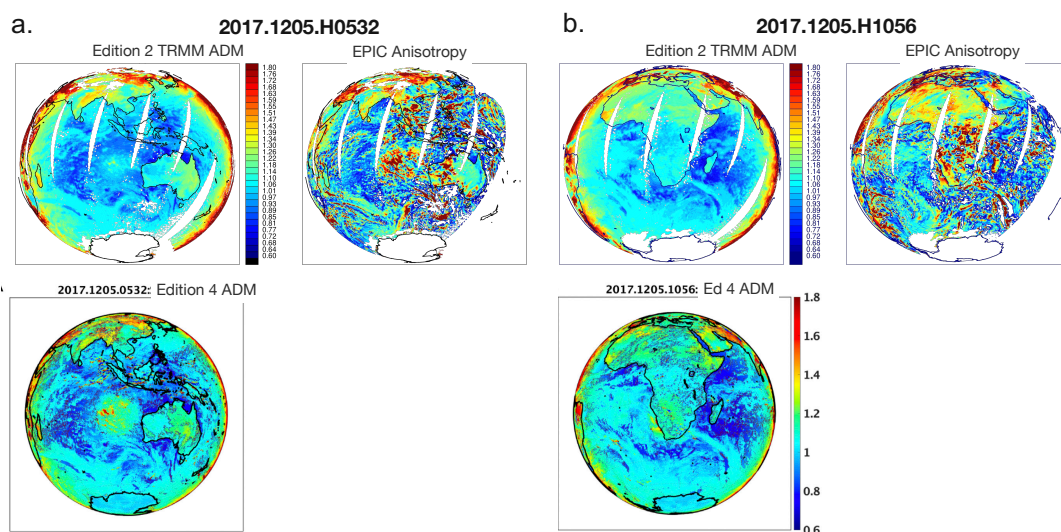
30

Figure A-1 Comparison of Anisotropy maps taken from Angular Distribution Model (ADM) tables on a) 5 December 2017 Hour 05.32 and on b) Hour 10.56. Shown are anisotropy maps using Edition 2 TRMM ADMs that we have constructed. Below are maps from Figure 9 of Su et al. 2021 constructed from Edition 4 ADMs. Also shown are 'EPIC anisotropies': anisotropies needed to match the EPIC AVIRIS reflected energy (SW EPIC-AVIRIS energy/CERES flux). For consistency we tried to match the same color table used in Figure 9.

References

Bovensmann, H., Burrows, J. P., Buchwitz, M., Frerick, J., Noël, S., Rozanov, V. V., Chance, K. V., and Goede, A. P. H.: SCIAMACHY: Mission Objectives and Measurement Modes, J. Atmos. Sci., 56, 127–150, 1999. 370

Carlson, B., Lacis, A., Colose, C., Marshak, A., Su, W., & Lorentz, S. (2019). Spectral signature of the Biosphere: NISTAR finds it in our solar system from the Lagrangian L-1 point. *Geophysical Research Letters*, 46, 10679– 10686. https://doi.org/10.1029/2019GL083736

Geogdzhayev, I.V., and A. Marshak, 2018: Calibration of the DSCOVR EPIC visible and NIR channels using MODIS and EPIC lunar observations. Atmos. Meas. Tech., 11, 359-368, doi:10.5194/amt-11-359-2018.

Green, R. O., et al. (1998), Imaging spectroscopy and the airborne visible/infrared imaging spectrometer (AVIRIS), Remote Sens. Environ., 65(3), 227–248.

Lim,Y.-K.; Wu,D.L.; Kim, K.-M.; Lee, J.N. An Investigation on Seasonal and Diurnal Cycles of TOA Shortwave Radiations from DSCOVR/ EPIC, CERES, MERRA-2, and ERA5. RemoteSens.2021,13,4595. https://doi.org/10.3390/rs13224595

Loeb, N. G., N. Manalo-Smith, S. Kato, W. F. Miller, S. K. Gupta, P. Minnis, and B. A. Wielicki, 2003: Angular Distribution Models for Top-of-Atmosphere Radiative Flux Estimation from the Clouds and the Earth's Radiant Energy System Instrument on the Tropical Rainfall Measuring Mission Satellite. Part I: Methodology. *J. Appl. Meteor. Climatol.*, **42**, 240–265, https://doi.org/10.1175/1520-0450(2003)042<0240:ADMFTO>2.0.CO;2.

Loeb, N.G., W. Su, D.R. Doelling, T. Wong, P. Minnis, S. Thomas, W.F. Miller, 5.03 - Earth's Top-of-Atmosphere Radiation Budget, Editor(s): Shunlin Liang, Comprehensive Remote Sensing, Elsevier, 2018, Pages 67-84,ISBN 9780128032213, https://doi.org/10.1016/B978-0-12-409548-9.10367-7

Marshak, A., J. Herman, A. Szabo, K. Blank, A. Cede, S. Carn, I. Geogdzhaev, D. Huang, L.-K. Huang, Y. Knyazikhin, M. Kowalewski, N. Krotkov, A. Lyapustin, R. McPeters, K. Meyer, O. Torres and Y. Yang, 2018. Earth Observations from DSCOVR/EPIC Instrument. Bulletin Amer. Meteor. Soc. (BAMS), 9, 1829-1850, https://doi.org/10.1175/BAMS-D-17-0223.1.

Ramaswamy, V., and S. M. Freidenreich (1991), Solar radiative line-by-line determination of water vapor absorption and water cloud extinction in inhomogeneous atmospheres, J. Geophys. Res., 96, 9133–9157.

Spurr, R. J. D., 2006: VLIDORT: A linearized pseudo-spherical vector discrete ordinate radiative transfer code for forward model and retrieval studies in multilayer multiple scattering media, J. Quant. Spectrosc. Radiat. Transfer, 102(2), 316-342, doi:10.1016/j.jqsrt.2006.05.005

Su, W., Liang, L., Doelling, D. R., Minnis, P., Duda, D. P., Khlopenkov, K., et al. (2018). Determining the Shortwave Radiative Flux from Earth Polychromatic Imaging Camera. J. Geophys. Res. Atmos. 123. doi:10.1029/2018JD029390

Su, W., Minnis, P., Liang, L., Duda, D. P., Khlopenkov, K., Thieman, M. M., Yu, Y., Smith, A., Lorentz, S., Feldman, D., and Valero, F. P. J.: Determining the daytime Earth radiative flux from National Institute of Standards and Technology Advanced Radiometer (NISTAR) measurements, Atmos. Meas. Tech., 13, 429–443, https://doi.org/10.5194/amt-13-429-2020, 2020.

Su W, Liang L, Duda DP, Khlopenkov K and Thieman MM (2021) Global Daytime Mean Shortwave Flux Consistency Under Varying EPIC Viewing Geometries. Front. Remote Sens. 2:747859. doi: 10.3389/frsen.2021.747859

Valero, F., A. Marshak, and P. Minnis (2021), Lagrange Point Missions: The Key to next Generation Integrated Earth Observations. DSCOVR Innovation, DSCOVR Innovation. Front. Remote Sens., 2, 745938, doi:10.3389/frsen.2021.745938

Wielicki, B. A., Barkstrom, B. R., Harrison, E. F., Lee, R. B., Louis Smith, G., and Cooper, J. E. (1996). Clouds and the Earth's Radiant Energy System (CERES): An Earth Observing System Experiment. Bull. Amer. Meteorol. Soc. 77, 853–868. https://doi.org/10.1175/1520-0477(1996)077<0853:CATERE>2.0.CO;2

5

We calculate the total amount of solar energy reflected by the earth from the EPIC camera onboard the DSCOVR satellite positioned 1.5 million km from earth. We compare it with
10   another estimate of the reflected energy from another instrument, NISTAR that is also on the DSCOVR satellite. Both energy estimates agree within the uncertainties of each instrument. Finally, we compare with a third estimate of solar reflected energy from the CERES instruments that are on board low-earth orbit satellites.